

# MedGAN: Medical Image Translation using GANs

Karim Armanious<sup>1,2</sup>, Chenming Yang<sup>1</sup>, Marc Fischer<sup>1,2</sup>, Thomas Küstner<sup>1,2,3</sup>, Konstantin Nikolaou<sup>2</sup>, Sergios Gatidis<sup>2</sup>, and Bin Yang<sup>1</sup>

<sup>1</sup>University of Stuttgart , Institute of Signal Processing and System Theory, Stuttgart, Germany

<sup>2</sup>University of Tübingen, Department of Radiology, Tübingen, Germany

<sup>3</sup>King's College London, Biomedical Engineering Department, London, England

arXiv:1806.06397v1 [cs.CV] 17 Jun 2018

**Abstract**—Image-to-image translation is considered a next frontier in the field of medical image analysis, with numerous potential applications. However, recent advances in this field offer individualized solutions by utilizing specialized architectures which are task-specific or by suffering from limited capacities and thus requiring refinement through non end-to-end training. In this paper, we propose a novel general purpose framework for medical image-to-image translation, titled MedGAN, which operates in an end-to-end manner on the image level. MedGAN builds upon recent advances in the field of generative adversarial networks (GANs) by combining the adversarial framework with a unique combination of non-adversarial losses which captures the high and low frequency components of the desired target modality. Namely, we utilize a discriminator network as a trainable feature extractor which penalizes the discrepancy between the translated medical images and the desired modalities in the pixel and perceptual sense. Moreover, style-transfer losses are utilized to match the textures and fine-structures of the desired target images to the outputs. Additionally, we present a novel generator architecture, titled CasNet, which enhances the sharpness of the translated medical outputs through progressive refinement via encoder-decoder pairs. To demonstrate the effectiveness of our approach, we apply MedGAN on three novel and challenging applications: PET-CT translation, correction of MR motion artefacts and PET image denoising. Qualitative and quantitative comparisons with state-of-the-art techniques have emphasized the superior performance of the proposed framework. MedGAN can be directly applied as a general framework for future medical translation tasks.

**Index Terms**—Generative adversarial networks, Deep neural networks, Image translation, PET attenuation correction, Motion correction.

## 1 INTRODUCTION

In the field of medical imaging, a wide range of methods is used to obtain spatially resolved information about organs and tissues in-vivo including plain radiography, computed tomography (CT), magnetic resonance imaging (MRI) and positron emission tomography (PET). The underlying physical principles are manifold producing imaging data of different dimensionality and of varying contrasts. This variety offers plentiful diagnostic options

but also poses a challenge when it comes to translation of imaging information between different modalities or different acquisitions within a modality.

Often enough, a situation occurs where two imaging modalities or image contrasts provide supplementary information so that two or more acquisitions are necessary for a complete diagnostic procedure. One example is hybrid imaging, e.g. PET/CT where CT is used for the technical purpose of attenuation correction (AC) of PET data [1]. Similarly, CT is used for dosimetry in radiation oncology and has to be acquired in addition to a diagnostic planning MR [2].

Additionally, optimization of image quality is an important step prior to the extraction of diagnostic information. Especially when using automated image analysis tools, high image quality is mostly required as input for the reliable generation of valid results. In specific situations, the generation of additional image information may be feasible without additional examinations using information from already acquired data. Therefore, a framework which is capable of translating between medical image modalities would shorten the diagnostic procedure by making additional scans unnecessary. This could prove to be beneficial not only for medical professionals but it also would be more convenient and efficient for patients alike.

Nevertheless, the task of translating from an input image modality to an output modality may seem to be problematic at first glance due to the possibility of introducing unrealistic information. This, of course, would render the synthetic image unreliable for use in diagnostic purposes. However, in specific technical situations, it is not the detailed image content in the synthetic image that is required but rather a global contrast property. An example is the use of CT data for PET AC where the CT image is not used directly for diagnosis. In other applications such as image quality optimization, the target image is more closely related to the input so that it seems at least possible to generate optimized image data that also preserve diagnostic information.

### 1.1 Related work

In the last decade, several computational methods have been introduced for the translation of medical images using machine learning approaches. For example, structured

Corresponding author: Karim Armanious  
E-mail address: karim.armanious@iss.uni-stuttgart.de

random forest was used in conjunction with an auto-context model to iteratively translate MR patches into corresponding CT for the purpose of PET AC [3]. For a given MR image, the synthetic CT patches are combined to give the final AC prediction. Going in a similar direction, pseudo-CT images were predicted from input MR patches using a k-nearest neighbour (KNN) regression algorithm. The efficiency of the prediction was first improved by local descriptors learned through a supervised descriptor learning (SDL) algorithm [4] and more recently through the combination of feature matching with learned non-linear local descriptors [5]. In another application domain, the correction of rigid and non-rigid motion artefacts in medical images could be viewed as a domain translation problem from motion-corrupted images into motion-free images. Kuestner et al [6] presented a method for cardiac and respiratory motion correction for PET images via simultaneously acquired MR motion model and a corresponding compressed sensing reconstruction scheme. A further interesting application is resolution enhancement of MR images. A super-resolution method, which translates a low-resolution MR image into a higher-resolution version, was developed based on a sparse representation framework which incorporates multi-scale edge analysis and a dimensionality reduction scheme for more efficient reconstruction [7].

Recently, the computer vision community has gained a lot of momentum in the area of medical image analysis [8]. This is due to recent advances in a range of applications such as lesion detection and classification [9], [10], semantic segmentation [11], [12], registration [13] and image enhancement [14]–[16] with the development of deep learning algorithms, especially the convolutional neural network (CNN) [17]. This has led to the development of several approaches for the generation and translation of image data. The most prominent of those is GAN.

In 2014, Ian J. Goodfellow [18] introduced his field changing technology titled Generative Adversarial Network (GAN). GANs are generative models with the objective of learning the underlying distribution of training data in order to generate new realistic data samples which are indistinguishable from the input dataset. Prior to the introduction of GANs, state-of-the-art generation models, such as Variational Autoencoders (VAE) [19], [20], tackled this task by performing explicit density estimation. In other words, the data generating distribution is explicitly defined and solved via mathematical approximations such as optimizing the lower bound of the likelihood instead of the intractable density function. In practice, VAEs produced blurry results which are easily distinguishable from the training dataset due to imperfect element wise measures and the injected noise during the training procedure [21]. GANs constitute an elegant alternative to explicit density estimation by simply defining a high-level goal such as "generate output data samples which are indistinguishable from input data" and minimizing the loss function through a second adversarial network instead of explicitly defining it.

GAN 的以实际结果为目标  
清晰且高效

The main underlying principle of GANs is that of rivalry and competition between two co-existing networks. The first network, the generator, takes random noise as input and outputs synthetic data samples. The second network, the discriminator, acts as a binary classifier which attempts to distinguish between real training data samples and fake synthetic samples from the generator. In the training procedure, the two networks are trained simultaneously with opposing goals. The generator is instructed to maximize the probability of fooling the discriminator into thinking the synthetic data samples are realistic. On the other hand, the discriminator is trained to minimize the cross entropy loss between real and generated samples, thus maximize the probability of correctly classifying real and synthetic images. Convergence is achieved by GANs from a game theory point of view by reaching Nash equilibrium [22]. Thus, the distribution of the generator network will converge to that of the training data and the discriminator will be maximally confused in distinguishing between real and fake data samples.

Due to its excellent performance in the generation of photo-realistic images, GAN has evoked much interest in the computer vision community. A large body of literature tracks the recent theoretical advancement of GANs [23], [24]. Alex Radford [25] made the natural extension of GANs from fully connected networks to CNNs by developing Deep Convolutional GANs (DC-GANs) in which both generator and discriminator are CNNs. DC-GANs replaces all the pooling layers with strided and fractional-strided convolutions and uses batch normalization and ReLU activation, which makes DC-GANs stable to train in most settings. However, GANs still suffers from some problems in the training procedure like gradient vanishing and instability [26]. To counteract such difficulties, researchers have proposed a series of modifications to the adversarial loss through the Wasserstein distance [27]–[29] in W-GAN and the MMD distance [30], [31] in MMD-GAN. Another suggested approach is the regularization of the discriminator during the training procedure. Naveen Kodali [32] pointed out that the excellent performance of W-GAN is due to the regularization of discriminator through the gradient penalty. Takeru Miyato [33] proposed in 2018 another approach called Spectral Normalization (SN-GAN) for the regularization of the discriminator which leads to more stabilization of the training procedure by normalizing the weights of the discriminator after every iteration. Moreover, David Berthelot [34] proposed a method called BE-GAN for the dynamic adjustment of weights in the adversarial loss to enforce the equilibrium between the generator and discriminator.

## 平衡

Researchers have adapted adversarial networks for a variety of tasks. Intuitively, GANs are the state-of-the-art model for image synthesis with recent models achieving unprecedented levels of image realism [35]. C. Ledig [36] achieved state-of-the-art results in the field of image super-resolution via the combination of the adversarial loss together with content loss in the Super-Resolution GAN (SR-GAN) framework. Other applications utilizing the

GANs includes classification [37], image denoising [38] and text to image synthesis [39] among many others. Perhaps the most relevant utilization of GAN in the field of medical image analysis is image-to-image translation.

In 2016, P. Isola [40] introduced the pix2pix GAN framework as general solution to supervised image-to-image translation problems. In this case, the generator receives as input an image from the input domain (e.g a grayscale photo) and is tasked to translate it to the target domain (e.g a coloured photo) by minimizing a pixel-reconstruction error (L1 loss) as well as the adversarial loss. On the other hand, the discriminator is tasked to differentiate between the fake output of the generator and the desired ground truth output image. Several modifications of this framework have been developed to enhance the quality of the output images. For example, PAN [41] replaced the pixel loss with a feature matching loss from the discriminator to reduce the blurriness of the output images. For the purpose of one-to-many translation, Fila-sGAN [42] utilized a pre-trained network for the calculation of style losses [43] to transfer the texture of input style images onto the translated image. Moreover, several unsupervised variants were introduced that do not require a dataset of paired input/target images for training, such as Cycle-GANs [44] and Disco-GANs [45].

Recently, GANs have been gaining more attention in the medical field. To represent a relatively complete overview of the current development of GANs in medical applications and showcase the impact of our proposed framework, we present this short review. D. Nie in [46] utilized the pix2pix architecture with an added gradient-based loss function for the translation from MR to CT images. This architecture suffered from limited modelling capacity due to patch-wise training. To circumvent the limitation that end-to-end training was not possible, it was required to train several GAN frameworks one after another via an auto-context model in-order to refine the results. A similar but unsupervised approach was used in [47] via Cycle-GANs. Pix2pix GANs were also utilized for the task of denoising low dose CT images by translating it into a high dose counterpart [48]. Additionally, [49] utilized a pre-trained network for the calculation of feature matching losses together with the Wasserstein distance loss. Synonymous with the above mentioned work, [50] utilized a largely similar architecture for the task of compressed sensing (CS) MRI reconstruction.

Perhaps most relevant to our work, [51] presented a generator architecture specifically tailored for the task of CS MRI reconstruction. The architecture consists of two residual networks concatenated in an end-to-end manner. Although the results of such an architecture surpassed that of conventional pix2pix, it suffers from the limitation of being specific to CS MRI reconstruction and not extendable to other translation tasks in which the target domain differs significantly from the input domain (e.g. MR to CT translation). Other medical translation tasks have also been recently explored such as CT to PET [52], CT to MRI [53] and 2T MR to 1T MR translation [54], [55].

## 1.2 Contributions

An analysis of the above mentioned machine learning and GAN-based methods identifies a common limitation. Specifically, existing approaches are designed with a particular application in mind or suffer from a limited modelling capacity. Thus, these models can not be easily applied to other medical translation tasks. Currently, there does not yet exist a framework which is optimized to jointly handle all the above mentioned medical translation tasks.

Based on this observation, we propose a unique general purpose GAN framework for medical image-to-image translation. Inspired by previous works such as ResNets [56], pix2pix, PAN and Fila-sGAN, our work combines the fragmented benefits of previous translation approaches with a novel generator architecture to create a none-tailored end-to-end solution capable of sharp detailed results on medical translation tasks.

Our contributions are summarized as follows:

- We propose the MedGAN framework as a general purpose solution for medical translation tasks. MedGAN captures the high and low frequency components of the desired target modality by combining the adversarial framework with a unique combination of non-adversarial losses. Specifically, we utilize a modified perceptual loss together with style-transfer losses.
- We present a novel generator architecture, which we title CasNet. Inspired by ResNets, this architecture chains together several fully convolutional encoder-decoder networks with skip connections into a single generator network. As the input medical image propagates through the encoder-decoder pairs, the translated images will progressively be refined and fine-tuned to ensure a high resolution and crisp output. Unlike existing generator architectures [51], CasNet is an end-to-end general purpose architecture not specific to any particular application.
- To showcase the effectiveness of our approach, we apply the MedGAN on three challenging and novel applications in medical diagnosis with no task-specific modifications to the hyperparameters. Namely, we translate from PET images into synthetic CT images, retrospective correction of motion artefacts by translating from motion-corrupted MR images to motion-free images and PET image denoising.
- We compare the results of the proposed framework against state-of-the-art models quantitatively and qualitatively. Also, we perform an analysis of individual loss components to prove that MedGAN is more than the sum of its parts.
- We tested the subjective perceptual performance and fidelity of the translated medical images by conducting a study in which 5 experienced radiologists where tasked to rate the results.

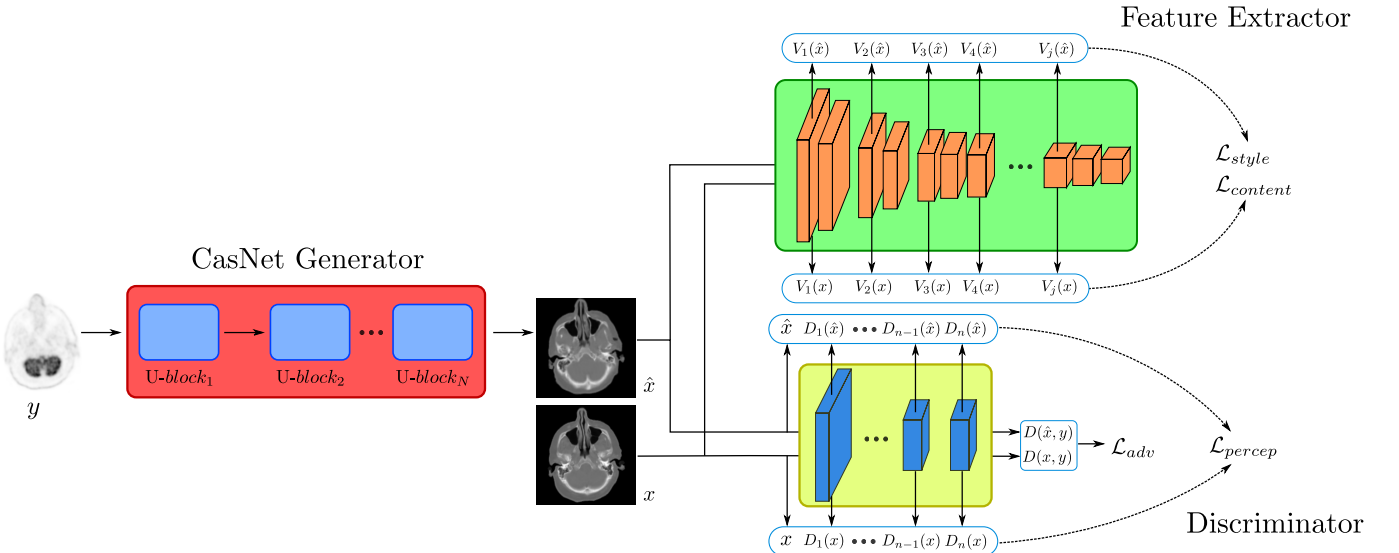


Fig. 1: Overview of the proposed MedGAN framework. MedGAN consists of a novel CasNet generator architecture as well as a discriminator and a pre-trained feature extractor. The generator  $G$  is tasked with translating input images from the source domain  $y$  (e.g PET) to the target domain  $\hat{x}$  (e.g. CT) through progressive refinement via encoder-decoder blocks. The adversarial discriminator  $D$  is trained to distinguish between real and transformed images as well as serving as a trainable feature extractor whose hidden layers are used to calculate the modified perceptual loss. The pre-trained feature extractor is used to extract deep rich features  $V_i(\hat{x})$  to calculate style transfer losses in order for the output to match the target’s style, textures and content.

## 2 MATERIALS AND METHODS

An overview of the proposed MedGAN framework for medical image-to-image translation tasks is presented in Fig. 1. MedGAN consists of three main components: a novel CasNet generator network, an adversarial discriminator network which also serves as a trainable feature extractor for the calculation of the perceptual loss, and a pre-trained feature extractor network for the calculation of style-transfer losses. In this section, the different loss components will be presented in details and the network architectures and training procedures will be illustrated starting first with some preliminary information.

### 2.1 Preliminaries

**2.1.1 Generative adversarial networks:** GANs consist of two main components, a generator and a discriminator. The generator  $G$  receives as input samples  $z$  from a prior noise distribution  $p_{\text{noise}}$  (e.g. a normal distribution) and is tasked to map it to the data space  $\hat{x} = G(z)$  inducing a model distribution  $p_{\text{model}}$ . On the other hand, the discriminator is a binary classifier whose objective is to classify data samples  $x$  from the data distribution  $p_{\text{data}}$  as real,  $D(x) = 1$ , and generated samples  $\hat{x}$  as fake,  $D(\hat{x}) = 0$ .

Both networks are pitted in a competition against each other with the generator attempting to produce generated samples which are indistinguishable from the real samples,  $p_{\text{model}} \sim p_{\text{data}}$ , thus fooling the discriminator. In the meantime, the discriminator’s objective is to avoid being fooled through learning meaningful features which distinguish real and generated samples. This concept of

adversary between opposing networks is well represented by the principles of game theory via a min-max optimization task which can be formulated as:

$$\min_G \max_D \mathcal{L}_{\text{GAN}} \quad (1)$$

where  $\mathcal{L}_{\text{GAN}}$  is the adversarial loss given by:

$$\mathcal{L}_{\text{GAN}} = \mathbb{E}_{x \sim p_{\text{data}}} [\log D(x)] + \mathbb{E}_{z \sim p_{\text{noise}}} [\log (1 - D(G(z)))] \quad (2)$$

The cost function of each network is dependent on the opposing network parameters, therefore convergence is achieved by reaching Nash equilibrium (i.e. saddle point) rather than a local minimum. The theoretically motivated approach of training the discriminator to optimality for a fixed generator using the above cost function usually results in a vanishing gradient problem. Empirically, it was found that alternating between updating the networks one at a time while fixing the other and maximizing  $\mathbb{E}_{z \sim p_{\text{noise}}} [\log D(G(z))]$  for the generator helps avoid this problem.

**2.1.2 Image-to-image translation:** The main principle of adapting GANs for image translation tasks is replacing the generator network by its **conditional variant (cGAN)**. In this case, the generator aims to map a source domain image  $y \sim p_{\text{source}}$  into its corresponding ground truth target image  $x \sim p_{\text{target}}$  via the mapping function  $G(y, z) = \hat{x} \sim p_{\text{model}}$ . This can generally be viewed as a regression task between two domains that share the same underlying structures but differ in surface appearance. However, instead of using manually constructed loss functions to measure the similarity between transformed and

target images in the data space, cGAN utilizes a binary classifier, the discriminator, as an elegant alternative of judging the quality of the output images.

In this case, the adversarial loss is rewritten as:

$$\mathcal{L}_{\text{cGAN}} = \mathbb{E}_{x,y} [\log D(x, y)] + \mathbb{E}_{z,y} [\log (1 - D(G(y, z), y))] \quad (3)$$

such that the discriminator aims to classify the concatenation of the source image  $y$  and its corresponding ground truth image  $x$  as real,  $D(x, y) = 1$ , while classifying  $y$  and the transformed image  $\hat{x}$  as fake,  $D(\hat{x}, y) = 0$ .

Nevertheless, image-to-image translation frameworks that rely solely on the adversarial loss function do not produce consistent results in the sense that the output images may not share a similar global structure as the desired ground truth image. In an effort to ensure that the transformed images do not significantly deviate from the source images, a pixel reconstruction loss, such as the L1 loss, is usually incorporated by current translation frameworks [40], [42] by calculating the mean absolute error (MAE) between the target and synthetic images:

$$\mathcal{L}_{\text{L1}} = \mathbb{E}_{x,y,z} [\|x - G(y, z)\|_1] \quad (4)$$

such that the final training objective is now given by:

$$\min_G \max_D \mathcal{L}_{\text{cGAN}} + \lambda \mathcal{L}_{\text{L1}} \quad (5)$$

where  $\lambda > 0$  is a weighting hyperparameter. Thus, in addition to fooling the discriminator, the generator must also match the transformed image to the target image in a pixel-wise sense hence, maintaining the global structure.

## 2.2 Perceptual loss

It is a well known fact that the **pixel reconstruction loss commonly leads to blurry results** [57], [58]. It is perhaps not surprising then that translation frameworks which utilize such loss functions often result in outputs with well maintained global structures at the cost of distortions and loss of details. Moreover, such loss function fails to capture the perceptual quality of human judgement. This is easy to imagine when examining two identical images shifted by a few pixels from each other. Unlike the human brain which will immediately capture the similarities between the images, a pixel-wise comparison will judge the images as vastly different [59]. This phenomenon is even more critical in the domain of medical images where small structures could significantly alter the diagnostic information of an image.

Thus, in an effort to capture the discrepancy between high frequency features representing the fine details while ensuring global consistency, we construct a perceptual loss based on the discriminator network which we utilize as a trainable feature extractor. The perceptual loss is calculated using the MAE between extracted feature representations:

$$P_i(G(y, z), x) = \frac{1}{h_i w_i d_i} \|D_i(G(y, z), y) - D_i(x, y)\|_1 \quad (6)$$

where  $D_i$  denotes the feature representations of the  $i^{\text{th}}$  hidden layer of the discriminator, and  $h_i$ ,  $w_i$  and  $d_i$  represents the height, width and depth of the feature space, respectively.

The perceptual loss can then be formulated as:

$$\mathcal{L}_{\text{perceptual}} = \sum_{i=0}^L \lambda_{pi} P_i(G(y, z), x) \quad (7)$$

with  $L$  the number of hidden layers of the discriminator and  $\lambda_{pi} > 0$  represents the influence of the  $i^{\text{th}}$  layer. The perceptual loss is used to train the generator such that it penalizes the perceptual differences between the images in addition to fooling the discriminator.

It is important to note that unlike other GAN frameworks which utilize feature matching losses (e.g. PAN [41]), the proposed perceptual loss does not eliminate the pixel reconstruction component since the MAE of the raw inputs ( $i = 0$ ) is included in Eq. (7). This is due to the empirical observation that penalizing the discrepancy in the pixel-space has a positive impact on the quality of the results and should not be ignored for the sake of strengthening the output details.

Additionally, in order to extract more meaningful features for the calculation of the perceptual loss, it was necessary to stabilize the training of the discriminator via spectral normalization [33]. This was achieved by normalizing the weight matrix  $\theta_{D,i}$  of each layer  $i$  in the discriminator:

$$\theta_{D,i} = \theta_{D,i} / \delta(\theta_{D,i}) \quad (8)$$

where  $\delta(\theta_{D,i})$  represents the spectral norm of the matrix  $\theta_{D,i}$ . As a result, the Lipschitz constant of the discriminator function  $D(x, y)$  will be constrained to 1. Practically, instead of applying singular value decomposition for the calculation of the spectral norm, an approximation via the power iteration method  $\hat{\delta}(W_i)$  was used instead in order to reduce the required computation complexity [33].

## 2.3 Style transfer losses

Image translation of medical images is a thoroughly challenging task since not only global fidelity is required but also high frequency crispness is a must to extract relevant medical information. For example, in PET to CT translation, the synthesized CT image must possess a detailed bone structure in order to be beneficial for PET attenuation correction. Furthermore, in the correction of MR motion artefacts, the resulting image must contain accurate soft-tissue structures as this will affect the results of further post-processing tasks such as segmentation and organ volume calculation.

In order to achieve the required level of details in the translated images, MedGAN incorporates non-adversarial losses from recent image style transfer techniques [59], [60] which transfer the style of an input image onto the output image matching their textures and details in the process. Similar to the perceptual loss, features from the

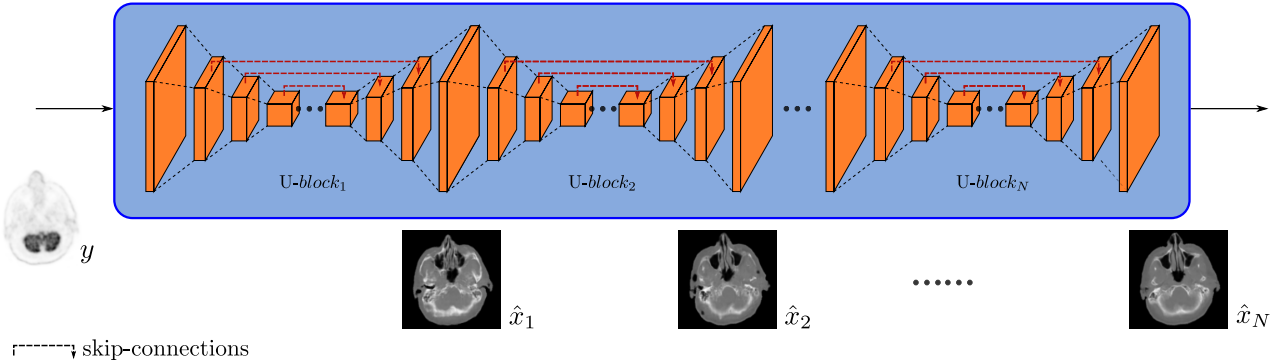


Fig. 2: The proposed CasNet generator architecture. CasNet concatenates several encoder-decoder pairs (U-blocks) to progressively refine the desired output image. This is done in an end-to-end manner regardless of the input image modality.

hidden layers of a deep CNN are used for loss calculations. However, instead of utilizing the discriminator as feature extractor, a pre-trained feature extractor is used. Compared to the discriminator, the pre-trained network has the advantage of being a much deeper neural network consisting of multiple convolutional blocks. This allows the extraction of deep rich features from a much larger receptive field which can be used to additionally enhance the global structures of the translated images in addition to the fine details.

**Style transfer losses can be divided into two main components: style loss and content loss.**

**Style loss:** The style loss is used to penalize the discrepancy in the style representations between the translated images and their corresponding target images. The style distribution can be captured by calculating the correlations between feature representations in the spatial extent. For instance,  $V_{j,i}(x)$  denotes the feature maps extracted from the  $j^{\text{th}}$  convolutional block and  $i^{\text{th}}$  layer of the feature extractor network for input image  $x$ . The feature maps have thus the size  $h_j \times w_j \times d_j$  with  $h_j, w_j, d_j$  being the height, width and spatial depth respectively. Typically, only the first layer of each convolutional block is used, thus the sub-index  $i$  is assumed to be 1 and will be omitted in the following notations. The feature correlations are represented by the Gram matrix  $Gr_j(x)$  of each convolutional block of the shape  $d_j \times d_j$ , whose elements are calculated by the inner product between feature maps over the height and width:

$$Gr_j(x)_{m,n} = \frac{1}{h_j w_j d_j} \sum_{h=1}^{h_j} \sum_{w=1}^{w_j} V_j(x)_{h,w,m} V_j(x)_{h,w,n} \quad (9)$$

The style loss is then calculated by summing up over all convolutional blocks the Frobenius squared norm of the difference between the correlations of the transformed images  $G(y, z)$  and their ground truth counterparts  $x$ :

$$\mathcal{L}_{\text{style}} = \sum_{j=1}^B \lambda_{sj} \frac{1}{4d_j^2} \|Gr_j(G(y, z)) - Gr_j(x)\|_F^2 \quad (10)$$

where  $\lambda_{sj} > 0$  are the hyperparameters representing the weight of the contribution of each of the convolutional blocks and  $B$  is the total number of convolutional blocks.

**Content loss:** The content loss directly penalizes the differences between feature representations extracted from the hidden layers of the feature extractor network. However, contrary to the style loss, the content loss does not capture discrepancies in style or texture, but it serves a similar purpose to the pixel-reconstruction loss by enhancing low frequency components and ensuring global consistency of the transformed images. The content loss is given by:

$$\mathcal{L}_{\text{content}} = \sum_{j=1}^B \lambda_{cj} \frac{1}{h_j w_j d_j} \|V_j(G(y, z)) - V_j(x)\|_F^2 \quad (11)$$

where again  $\lambda_{cj} > 0$  are the hyperparameters representing the influence of the first layer of each convolutional block.

## 2.4 MedGAN architecture

**2.4.1 U-blocks:** The task of image-to-image translation can be described as mapping a high dimensional input tensor into an output high dimensional tensor with different surface appearance but of the same underlying structure. From another aspect, the main architectural consideration of the MedGAN framework is robustness to all medical image modalities. MedGAN must not be tailored to any specific medical image transformation task. Therefore, the fundamental building block of the proposed MedGAN framework was chosen to be an encoder-decoder architecture, which we title a U-block.

A U-block is a fully convolutional encoder-decoder network following the architecture introduced in [40]. It is inspired by U-nets [61] which have been adapted according to the architectural guidelines in [25] to stabilize the adversarial training process. The encoding path maps the image from the input domain, in  $256 \times 256$  resolution, into a high level representation using a stack of 8 convolutional layers each followed by batch normalization and Leaky-ReLU

activation functions. The number of convolutional filters is 64, 128, 256, 512, 512, 512, 512 and 512 respectively with kernel size  $4 \times 4$  and stride 2. For the desired purpose of medical image translation, stochasticity is not desired and the encoding path only receives the source domain image  $y$  as input. As a result, the subscript  $z$ , in Eq. (3), denoting input noise samples will hence be omitted from future notations. The decoding path mirrors the encoding architecture albeit utilizing fractionally strided deconvolutions. This enlarges the resolution by a factor of two after each layer, which inverts the downsampling by the encoding path and maps from the high level representation into the output image domain. The upsampling path consists of 512, 1024, 1024, 1024, 512, 256 and 128 filters, respectively, in each of the layers which utilize ReLU activation functions except for the last deconvolutional layer which uses a Tanh activation instead.

Additionally, a U-block contains skip-connections which always concatenate spatial channels between mirrored layers in the encoder and decoder paths, e.g. between the 2<sup>nd</sup> encoding layer and the 7<sup>th</sup> decoding layer. These connections are fundamental for image transformation tasks since they pass critical low level information between the input and output images which will otherwise be lost through the bottleneck layer leading to severe degradation in output quality.

**2.4.2 CasNet:** Translation of medical images poses a more strenuous challenge compared to regular image transformation tasks due to the high amount of relevant medical information contained in small detailed structures in the images which can easily be lost or distorted during the translation process. In order to circumvent this issue, current approaches utilize either specialized architectures for a given medical transformation task [51] or require the training of several frameworks one after the other [46]. In order to construct a general purpose end-to-end network which is more capable of transforming medical images we propose the CasNet architecture presented in Fig. 2.

Inspired by ResNets [56], which cascades the so-called residual blocks, CasNets increases the generative capabilities of MedGAN by concatenating several U-blocks in an end-to-end manner. This is done such that the output image of the first U-block is passed as input to the second block till the  $N^{\text{th}}$  block. As a result, the medical translation task is now divided among the U-blocks and the desired target domain output is progressively refined as it passes through the encoder-decoder pairs. Backpropagation of the loss gradients through such network depth may result in a vanishing gradient problem. However, due to the utilization of skip connections in the U-blocks this problem is mitigated. Empirically, this was found to be an effective solution to arbitrary increasing the network capacity while maintaining training stability in comparison to a single U-net of increasing depth.

Although CasNets and ResNets share the same basic principle of concatenating a more basic building block, fundamental differences exist between the two networks.

The first is concerning the depth. Residual blocks consist of only 2-4 convolutional layers whereas U-blocks have a deeper architecture of 16 convolutional layers which greatly increase the generative capacity of CasNets. Moreover, CasNets utilize intermediate skip connections to pass low level information and prevent vanishing gradients instead of using identity mappings to connect the input image to the output of the residual block.

**2.4.3 Discriminator architecture:** For the discriminator, we utilize a modified encoding architecture similar to the PatchGAN architecture proposed in [40]. Instead of classifying the target and output images as being real or not, PatchGAN is designed to have a reduced receptive field such that it divides the input images convolutionally into smaller image patches before classifying them and averaging out the result. As a result, the discriminator's attention is restricted to small image patches which encourage high frequency correctness and enables detailed outputs by the generator. Generally,  $70 \times 70$  patches is the conventional patch size to utilize in order to avoid the typical tiling artefacts with smaller patch sizes. However, we empirically found that the utilization of smaller patches in combination with the previously introduced non-adversarial losses, e.g. perceptual and style transfer losses, promotes sharper results while eliminating conventional tiling artefacts. As a result, we utilize a  $16 \times 16$  patch size by incorporating two convolutional layers with 64 and 128 spatial filters followed by batch normalization and Leaky-ReLU activation functions. Lastly, to output the required confidence probability map, a convolution layer of output dimension 1 and a sigmoid activation function is used.

## 2.5 MedGAN framework and training

In summary, our MedGAN framework consists of a CasNet generator network penalized from the perceptual and pixel perspectives via an adversarial discriminator network while utilizing a pre-trained feature extractor to ensure that translated output matches the desired target image in style, texture and content. The framework is trained via a min-max optimization task using the following cumulative loss function:

$$\mathcal{L}_{\text{MedGAN}} = \mathcal{L}_{\text{cGAN}} + \lambda_1 \mathcal{L}_{\text{perceptual}} + \lambda_2 \mathcal{L}_{\text{style}} + \lambda_3 \mathcal{L}_{\text{content}} \quad (12)$$

where  $\lambda_1$ ,  $\lambda_2$  and  $\lambda_3$  balance out the contribution of the different loss components. As a result of extensive hyper-parameter optimization, we utilize  $\lambda_1 = 20$  and  $\lambda_2 = \lambda_3 = 0.0001$ . Regarding the feature extractor, we use a deep VGG-19 network pre-trained on ImageNet classification task [62]. It consists of 5 convolutional blocks, each of 2-4 layers, and three fully connected layers. Although it is pre-trained on non-medical images, the features extracted by the VGG-19 network was found to be beneficial in representing the texture and style information as will be

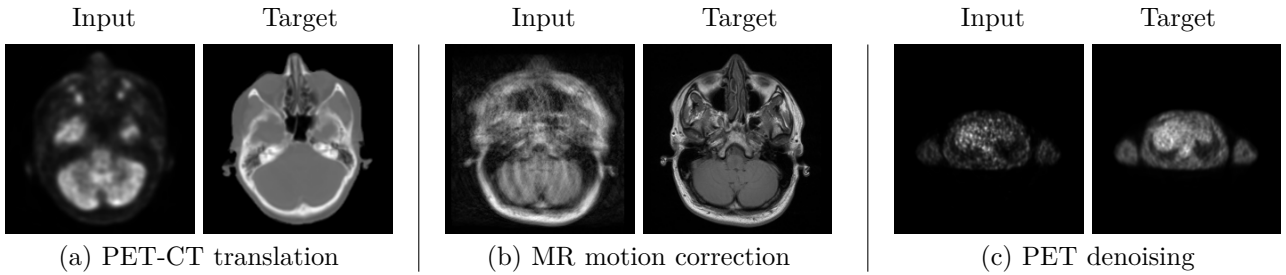


Fig. 3: An example of the three datasets used for the qualitative and quantitative evaluation of the MedGAN framework.

**Algorithm 1** Training pipeline for MedGAN

---

**Require:** Paired training dataset  $\{(x_l, y_l)\}_{l=1}^T$   
**Require:** Number of training epochs  $N_{\text{epoch}} = 200$ ,  
 number of training iterations for generator  $N_G = 3$ ,  
 $\lambda_1 = 20$  and  $\lambda_2 = \lambda_3 = 0.0001$   
**Require:** Load pretrained VGG-19 network parameters  
**Initialize:** Weight parameters of generator and discriminator  $\theta_G, \theta_D$

```

1: for  $n = 1, \dots, N_{\text{epoch}}$  do
2:   for  $l = 1, \dots, T$  do
3:     for  $t = 1, \dots, N_G$  do
4:        $\mathcal{L}_{\text{cGAN}} \leftarrow -\log(D(G(y_l), y_l))$ 
5:        $\mathcal{L}_{\text{perceptual}} \leftarrow \sum_i \lambda_{pi} P_i(G(y_l), x_l)$ 
6:        $\mathcal{L}_{\text{style}} \leftarrow \sum_j \frac{\lambda_{sj}}{4d_j^2} \|Gr_j(G(y_l)) - Gr_j(x_l)\|_F^2$ 
7:        $\mathcal{L}_{\text{content}} \leftarrow \sum_j \frac{\lambda_{cj}}{h_j w_j d_j} \|V_j(G(y_l)) - V_j(x_l)\|_F^2$ 
8:        $\theta_G \leftarrow -\nabla_{\theta_G} [\mathcal{L}_{\text{cGAN}} + \lambda_1 \mathcal{L}_{\text{perceptual}} + \lambda_2 \mathcal{L}_{\text{style}} + \lambda_3 \mathcal{L}_{\text{content}}]$ 
9:     end for
10:     $\mathcal{L}_{\text{cGAN}} \leftarrow \log(D(x_l, y_l)) + \log(1 - D(G(y_l), y_l))$ 
11:     $\theta_D \leftarrow \nabla_{\theta_D} [\mathcal{L}_{\text{cGAN}}]$ 
12:    Spectral normalization:  $\theta_{D,i} = \theta_{D,i}/\delta(\theta_{D,i})$ 
13:  end for
14: end for

```

---

shown in the following results section. For training, we make use of the **ADAM** optimizer [63] with momentum value of 0.5 and a learning rate of 0.0002. We apply instance normalization [64], with batch size of 1, which was shown to be beneficial for image transformation tasks. For the optimization of MedGAN, we train the patch discriminator once for every three iterations of training the CasNet generator. We empirically found that this leads to a more stable training and produces higher quality results. The entire training process is illustrated in Algorithm 1. As a result of a time consuming hyperparameter optimization,  $\lambda_{pi}$  was chosen to allow both layers of the discriminator to have equal influence on the loss. Similarly,  $\lambda_{cj}$  was set to allow all but the deepest convolutional blocks to influence the content loss. However, the style loss  $\lambda_{sj}$  was chosen to include only the influence of the first and last convolutional blocks of the pre-trained VGG-19 network.

The MedGAN framework was trained on a single Nvidia Titan-X Gpu with a CasNet generator architecture consisting of  $N = 6$  U-blocks. The training time is largely dependent on the size of the dataset used but was found to be an average of **36 hours**. The inference time, however,

was found to be 115 milliseconds for each test image.

## 3 EXPERIMENTAL EVALUATIONS

## 3.1 Datasets

The MedGAN framework was designed with an objective of being an end-to-end general purpose solution for medical image translation problems. To showcase this capability, we train MedGAN on three novel and challenging medical applications with no task-specific changes to the hyperparameters and model architecture. The utilized datasets are illustrated in Fig. 3.

For the first application, we translate from PET images into corresponding synthetic CT images. This is a challenging task since the target modality contains more detailed information, e.g. bone structures and soft tissues, compared to the input source modality. For that purpose, we used an anonymized dataset of 46 patients of the brain region acquired on a joint PET/CT scanner (SOMATOM mCT, Siemens Healthineers, Germany). The CT data has an original resolution of  $0.85 \times 0.85 \times 5 \text{ mm}^3$  and a matrix size of  $512 \times 512$ , while PET data have a voxel size of  $2 \times 2 \times 3 \text{ mm}^3$  and a matrix size of  $400 \times 400$ . The resolution of both modalities was resampled to a voxel size of  $1 \times 1 \times 1 \text{ mm}^3$  and then aligned using the header information and centre cropped to extract the relevant head region. Due to hardware limitations, only 2-dimensional axial slices of resolution  $256 \times 256$  pixels were used during the training procedure, with a dataset of 1935 paired training images from 38 patients, and 414 images from 8 separate patients for validation.

The second application is concerned with the retrospective correction of motion artefacts in MR images. First initial results using a VAE architecture with VGG-based perceptual loss was showed in [65]. We translate from motion-corrupted MR images into their corresponding motion-free images. This is a challenging task, not only because of the severity of rigid motion artefacts in the acquired datasets but also because of the difficulty achieving pixel-wise alignment between motion free and motion corrupted MR scans taken sequentially in time. Therefore, this experiment serves the purpose of showcasing the robustness of the proposed MedGAN framework against alignment errors in the required training datasets. An anonymized dataset of 11 volunteers from the brain region was acquired using a clinical MR scanner (Biograph mMR 3 Tesla, Siemens Healthineers, Germany). A T1-weighted spin echo (SE) sequence was acquired one under

resting conditions and once under motion of the head in all volunteers [66]. Similar to the PET-CT dataset, the MR data was scaled to a spacing of  $1 \times 1 \times 1\text{mm}^3$  and 2D axial slices of  $256 \times 256$  resolution was extracted from the brain region. Image data were paired in that a motion-free and a motion-corrupted image were acquired and aligned using the header information. The training datasets consisted of 1445 MR images from 7 patients, while evaluation was carried out on a separate dataset of 556 images from 4 patients.

For the final application of this study, we utilize the MedGAN framework for direct denoising of PET imaging data. For this study anonymized datasets were used for the head, torso and abdomen regions from 33 patients using a PET scanner (Biograph mCT, Siemens Healthineers, Germany). The scans have a resolution of  $2.8 \times 2.8 \times 2\text{mm}^3$  and a volume of  $256 \times 256 \times 479$ . Noisy PET scans were produced by reconstructing PET images from only 25 % of the original acquisition time and original PET scans were paired together in a dataset of 11420 training 2D axial slices and 4411 validation images.

### 3.2 Experimental setup

**3.2.1 Analysis of loss functions:** In addition to the conditional adversarial loss, the MedGAN framework incorporates a unique combination of multiple non-adversarial losses as part of its framework, namely the perceptual, style and content losses. This combination of different loss functions is essential to capture the low frequencies, ensuring global consistency, as well as the high frequency details of the desired target images. In order to prove that MedGAN is more than the sum of its parts, as well as the impact of individual loss components, in the first set of experiments we train separate models for the task of PET to CT translation each utilizing individual loss components in comparison with the MedGAN framework. For a fair comparison, all trained models utilized identical architectures consisting of a single U-block generator and a  $16 \times 16$  patch discriminator network, except for MedGAN which utilized a CasNet architecture of 6 U-blocks. Moreover, the models were trained for the same duration of 200 epochs with three generator updates for each discriminator update and identical hyperparameter settings. Additionally, to showcase that MedGAN's optimized performance is not only due to the increased capacity provided by the CasNet architecture but also the unique combination of non-adversarial losses, a MedGAN framework consisting of a single U-block generator, abbreviated MedGAN-1G, was also trained.

**3.2.2 Comparison with state-of-the-art techniques:** Existing medical image translation approaches suffer from the drawback of either using specialized architectures which are task-specific and not easily adaptable to other translation applications [51] or being patch based and requiring refinement through iterative training [46]. The MedGAN framework was designed with the main objective

of overcoming such limitations by being an end-to-end general purpose solution for medical image translation tasks. To prove this capability, in the second set of experiments several state-of-the-art approaches where re-implemented, trained on the three acquired datasets and compared qualitatively and quantitatively with the MedGAN framework.

First, the cGAN loss was combined with an L1 pixel reconstruction loss into the pix2pix framework which is a general framework for translation tasks [40]. This method was used previously for various medical applications such as MR to CT translation [46], CT denoising [48] and 2T to 1T MR translation [54]. Moreover, a perceptual adversarial network (PAN) [41] was also implemented which incorporates a similar perceptual loss component as the one proposed by MedGAN. However, fundamental differences exists between the two frameworks. The perceptual loss utilized within the MedGAN framework incorporates a pixel loss component by calculating the MAE of the raw inputs as well as that of the hidden features extracted by the discriminator. Empirically, we found this component to be vital to ensure global consistency of the translated images. Additionally, PAN penalizes the discriminator to preserve the perceptual discrepancy between the hidden features in order to stabilize training. However, in our experimentations we found out that such a penalty term often leads to blurred or reduced details in the resultant medical images. The Fila-sGAN has a different objective compared to MedGAN. It attempts to transfer the textures of an input style image onto a GAN translated image in order to generate multiple variations of the same underlying structure [42]. However, it is similar to our approach in that it utilizes a pre-trained VGG network to calculate style and content losses in addition to a total variation loss and a L1 pixel reconstruction loss. Therefore, we re-implement Fila-sGAN with the objective of enhanced image translation by replacing the style input images with the original source domain images. The final translation approach used in this comparative study is the ID-CGAN which was designed for the denoising of weather artefacts in natural images [38]. ID-CGAN incorporates a combination of the adversarial loss, L2 pixel reconstruction loss and the content loss extracted from a pre-trained VGG-19 network. For fair comparison, all methods were trained using the same settings, hyperparameters and architecture (a single U-block generator and patch discriminator) as the MedGAN framework which only differed in utilizing the novel CasNet generator architecture of 6 U-blocks.

**3.2.3 Perceptual study and validation:** Moreover, to judge the fidelity of the translated images, we conducted a series of experiments in which 5 experienced radiologists were presented a series of trials each containing the ground truth target image, the MedGAN output as well as the pix2pix output. In each of the trials, the images appeared in a randomized order and participants were asked to classify which was the ground truth image as well as

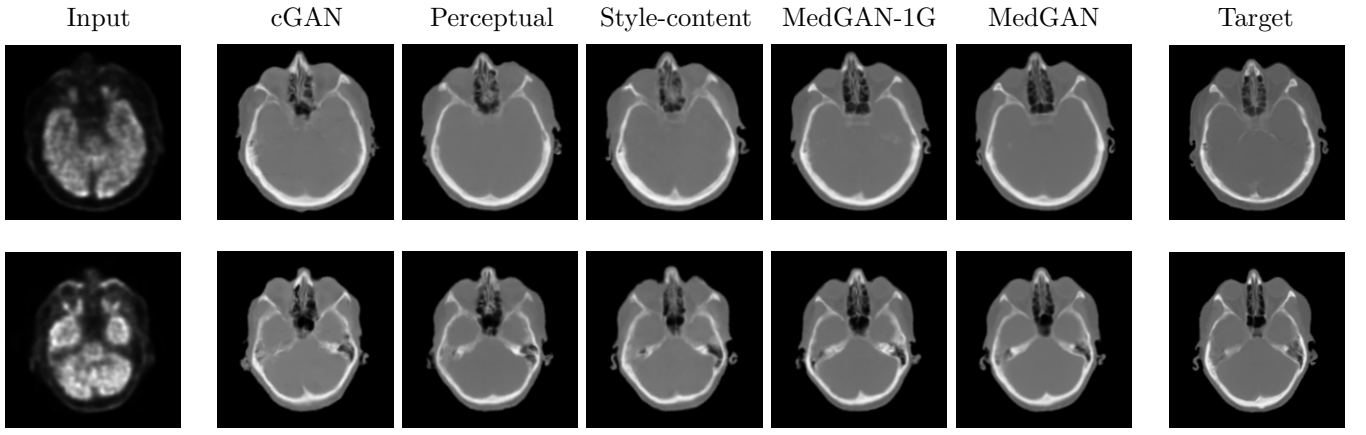


Fig. 4: Comparison of the effectiveness of different loss functions used within the MedGAN framework. On the leftmost column, input PET images are given which corresponds to the ground truth CT images given in the rightmost column in two slices. Intermediate columns show synthetically translated CT images as a result of training under different loss components.

rate the quality of each image using a 4-point score, with 4 being the most realistic. Each participant tested one translation application at a time and was presented 60 triads of images from that respective dataset. All images were presented in  $256 \times 256$  resolution.

### 3.3 Evaluation metrics

The performance of the MedGAN framework was evaluated on the above-mentioned datasets both qualitatively and quantitatively. With respect to quantitative experiments, there is no consensus in the scientific community regarding the best evaluation metrics to asses the performance of generative models [67]. Therefore, we utilize several traditional image quality metrics to judge the quality of the translated medical images from different perspectives such as Structural Similarity Index (SSIM) [68], Peak Signal to Noise Ratio (PSNR), Mean Squared Error (MSE), Visual Information Fidelity (VIF) [69] and Universal Quality Index (UQI) [70]. Nevertheless, recent studies pointed out that these metrics could not be counted upon solely as reference for human judgement of image quality. Hence, we additionally utilize a state-of-the-art metric titled Learned Perceptual Image Patch Similarity (LPIPS) which was reported to outperform previous metrics as a perceptual metric of quality [71]. For the qualitative comparisons, we present the input, transformed and ground-truth target images.

## 4 RESULTS

### 4.1 Analysis of loss functions

The qualitative and quantitative results of utilizing individual loss functions in comparison to the MedGAN framework are presented in Fig. 4 and Table I respectively. From a qualitative point of view, we found that the traditional adversarial loss  $\mathcal{L}_{\text{cGAN}}$  leads to the worst results (Fig. 4). This is also reflected in the quantitative scores (Table I) where cGAN achieves the worst numerical scores across the chosen metrics. On the other hand, utilizing

TABLE I  
Quantitative comparison of loss components

	Loss	SSIM	PSNR(dB)	MSE	VIF	UQI	LPIPS
cGAN	0.8960	23.65	313.2	0.3858	0.9300	0.2592	
Perceptual	0.9071	24.20	287.0	0.4183	0.9514	0.2628	
Style-content	0.9046	24.12	282.8	0.4105	0.9435	0.2439	
MedGAN-1G	0.9121	24.51	271.8	0.4348	<b>0.9569</b>	<b>0.2142</b>	
MedGAN	<b>0.9160</b>	<b>24.62</b>	<b>264.6</b>	<b>0.4464</b>	0.9558	0.23015	

the discriminator as a trainable feature extractor for the calculation of the perceptual loss improves the results by enhancing the global consistency due to the pixel-wise component of the loss, as well as enhancing the details of the resultant bone structures. However, when compared to the ground truth target images, it is observed that the translated CT images have a reduced level of details. Combining the generative framework with a pre-trained feature extractor (VGG-19) for the calculation of style and content losses further improved the qualitative results, where the translated images have an enhanced level of details and more fine-tuned structures due to matching the target's texture and global content. The utilization of MedGAN-1G, with a single U-block generator architecture, results in an increased sharpness of the translated images as well as a notable improvement of the quantitative metrics compared to the individual loss components. Yet, incorporating the CasNet generator architecture to progressively refine the translated CT images further enhances the output of the MedGAN framework with more refined bone structures and details. As shown in Table I, this is reflected by a significant reduction in the MSE as well as increases in the SSIM, PSNR and VIF compared to MedGAN-1G with a subtle difference in the UQI score and reduction in LPIPS score.

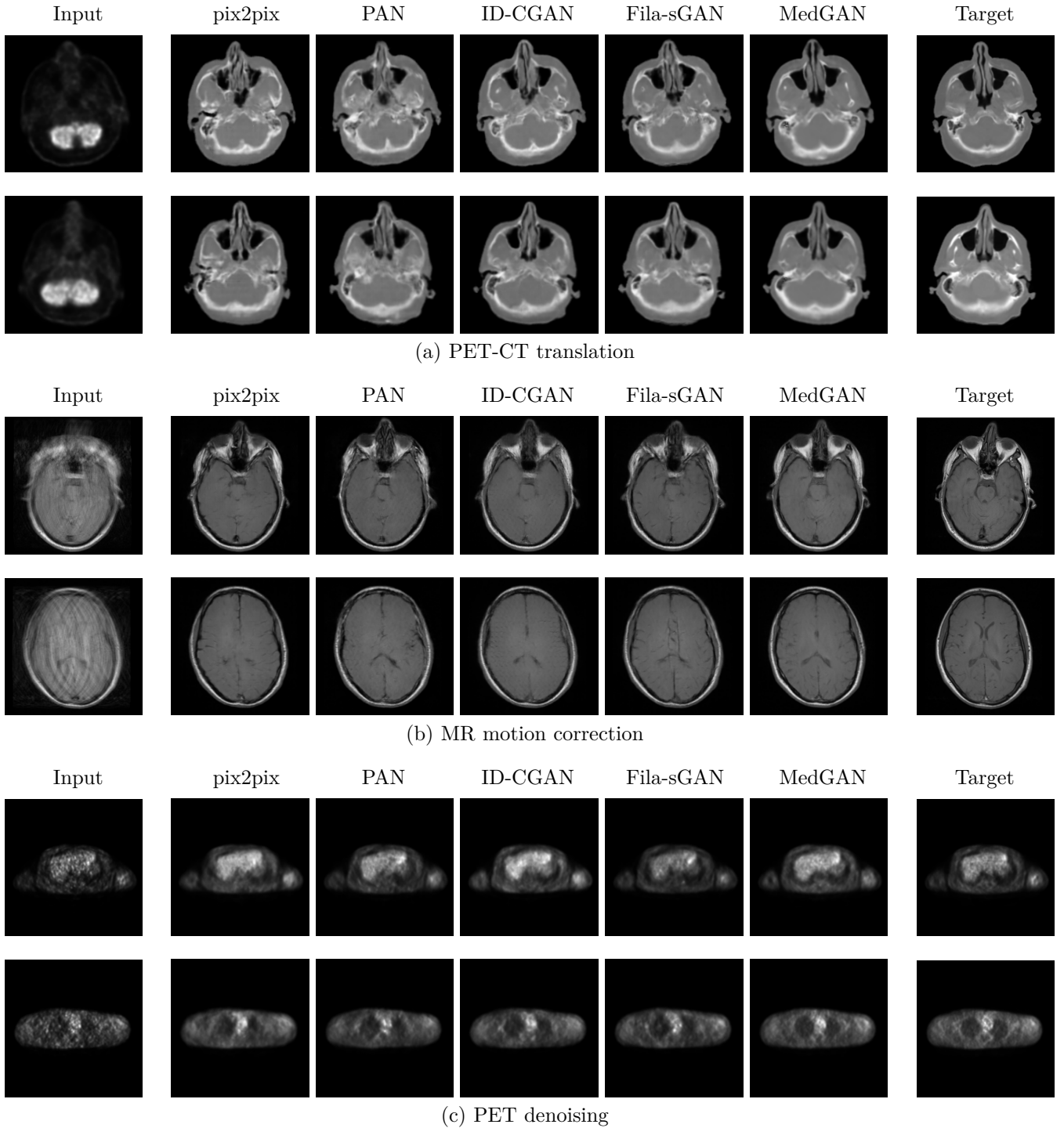


Fig. 5: Comparison of the applicability of MedGAN and different state-of-the-art techniques as general purpose solution for various medical image translation tasks in two respective image slices of each task.

#### 4.2 Comparison with state-of-the-art techniques

For the second set of experiments, we compared the performance of MedGAN against several state-of-the-art translation frameworks including pix2pix, PAN, ID-CGAN and Fila-sGAN. The results are given in Fig. 5 and Table II for the qualitative and quantitative comparisons respectively. Pix2pix produced the worst results of the implemented methods with PAN only slightly outperforming it. Although they partially succeeded in capturing the

underlying structure of the motion corrupted MR images (Fig. 5 (b)), in PET to CT translation the output images lacked sharpness and homogeneity, including realistic bone structures. This is also reflected quantitatively with these methods achieving the worst scores in Table II. ID-CGAN outperformed the previous methods in the task of PET to CT translation with the resultant images having a more consistent global structure. However, ID-CGAN did not perform as strongly on the other datasets. For example,

TABLE II  
Quantitative comparison with state-of-the-art frameworks

Method	(a) PET-CT translation						(b) MR motion correction						(c) PET denoising					
	SSIM	PSNR(dB)	MSE	VIF	UQI	LPIPS	SSIM	PSNR(dB)	MSE	VIF	UQI	LPIPS	SSIM	PSNR(dB)	MSE	VIF	UQI	LPIPS
pix2pix	0.9017	23.93	299.2	0.4024	0.9519	0.2537	0.8138	23.79	335.2	0.3464	0.5220	0.2885	0.9707	34.89	37.20	0.6068	0.9440	0.0379
PAN	0.9027	24.10	292.2	0.4084	0.9190	0.2582	0.8116	23.91	311.4	0.3548	0.5399	0.2797	0.9713	34.97	38.76	0.6068	0.9431	0.0348
ID-CGAN	0.9039	24.13	288.6	0.4059	0.9389	0.2423	0.8214	<b>24.26</b>	289.8	0.3685	0.5855	0.2747	0.9699	34.28	39.45	0.6023	0.9435	0.0346
Fila-sGAN	0.9039	24.08	289.6	0.4146	0.9054	0.2320	0.8114	23.91	318.7	0.3431	0.4957	0.2570	0.9726	35.05	35.80	<b>0.6279</b>	<b>0.9472</b>	0.0328
MedGAN	<b>0.9160</b>	<b>24.62</b>	<b>264.6</b>	<b>0.4464</b>	<b>0.9558</b>	<b>0.2302</b>	<b>0.8363</b>	24.18	<b>289.9</b>	<b>0.3735</b>	<b>0.6037</b>	<b>0.2391</b>	<b>0.9729</b>	<b>35.23</b>	<b>33.54</b>	0.6168	0.9443	<b>0.0292</b>

ID-CGAN resulted in significant tilting artefacts as well as blurred output details in the task of MR motion correction. Fila-sGAN similarly produced inconsistent results on the different datasets, for while it produced acceptable results in PET to CT translation, it resulted in blurred denoised PET images (Fig. 5 (c)) as well as unrealistic textures in the motion correction MR images. The MedGAN framework surpassed the previously mentioned methods on the three different translation tasks producing sharper and more homogeneous outputs from the visual perspective. This superior performance was also reflected quantitatively in Table II with MedGAN generally outperforming the other methods on the different translation tasks.

#### 4.3 Perceptual study and validation

The results of the perceptual study conducted by radiologists on the three utilized datasets are presented in Table III. The final column of this table states the percentage of images classified by radiologists as real out of the triad of presented images. In the PET to CT translation, 25.3 % of the synthetically generated CT images by the MedGAN framework managed to fool radiologists into thinking they are ground truth images from a real CT scanner. In MR motion correction and PET denoising, the percentage of MedGAN images classified as real was 6.7 % and 14.3 % respectively. Additionally, radiologists rated the output of the MedGAN framework highly with a mean score of 3.22 in comparison to 1.70 achieved by pix2pix and 3.81 by the ground truth images. The superior performance of MedGAN was also reflected in the remaining two applications, were MedGAN achieved a mean score of 2.81 in comparison to 1.98, and a score of 3.02 in comparison to 1.73 by pix2pix in MR motion correction and PET denoising, respectively.

## 5 DISCUSSION

In this work, we presented MedGAN as an end-to-end general purpose solution for medical image translation tasks. MedGAN incorporates a novel combination of non-adversarial losses, namely the perceptual and style-content losses, on top of an adversarial framework to capture the high and low frequency components of the target images. The proposed framework utilized the CasNet architecture, a novel generator network which progressively refines the

TABLE III  
Results of perceptual study

Method	(a) PET-CT translation		
	mean	SD	real %
pix2pix	1.70	0.531	0.00
MedGAN	3.22	0.590	25.3
Ground truth	3.81	0.394	74.7
Method	(b) MR motion correction		
	mean	SD	real %
pix2pix	1.98	0.514	0.00
MedGAN	2.81	0.573	6.70
Ground truth	3.87	0.337	93.3
Method	(c) PET denoising		
	mean	SD	real %
pix2pix	1.73	0.511	0.00
MedGAN	3.02	0.542	14.3
Ground truth	3.70	0.461	85.7

translated image via encoder-decoder pairs in an end-to-end manner. This leads to homogeneous and realistic global structures as well as fine-tuned textures and details which are especially important in the domain of medical images.

The proposed MedGAN framework is more than the sum of its part. An analysis performed on the task of PET to CT translation, presented in Fig. 4 and Table I, highlighted the fact that MedGAN surpasses the performance of its individual loss components. cGAN results in the worse performance both qualitatively and quantitatively. Specifically, the resulting CT images of this method have a largely non-homogeneous global structure compared to the desired ground truth images. A good example would be examining the bone structures of the nose region in the resultant images. Comparatively, the utilization of the perceptual loss and the style-content losses resulted in an overall improved performance. However, it was observed that the style-content losses have a more significant impact upon the quality of the resultant images. Nevertheless, this impact is not reflected in the quantitative results in Table I where the perceptual loss generally excels in comparison. This may be attributed to the reported fact that the quantitative scores may not always reflect the perceptual quality of human judgement [71]. The proposed

MedGAN framework combines all above mentioned benefits of individual loss components, as it jointly ensures global homogeneity of the resultant images as well as enhancing the level of details and matching the textures and fine structures of the target images. This improvement is not only the result of the increased capacity provided by the CasNet architecture. MedGAN-1G, with a single U-block generator, also surpassed qualitatively and quantitatively the results of individual loss components, which are trained using an identical architecture to it. However, the reduced capacity of MedGAN-1G results in a slight degradation of the quality of translated images compared to MedGAN, which utilizes a CasNet architecture of 6 U-blocks. Further analysis of the performance of the CasNet architecture is presented in Appendix A.

To showcase the capability of MedGAN as a general purpose framework for medical image translation tasks, we applied MedGAN on three novel and challenging applications which are PET to CT translation, correction of motion artefacts in MR images and PET denoising. Moreover, we compared MedGAN's performance on the above mentioned tasks against several state-of-the-art translation techniques and compared the results qualitatively and quantitatively. In the task of PET to CT translation, MedGAN produced highly realistic and homogeneous bone structures in the resultant CT images that closely matched the ground truth CT images and surpasses visually those produced by ID-CGAN and Fila-sGAN. In the task of MR motion correction, the resultant synthetic MR images are artefact-free and with highly realistic textures and fine-structures. Finally, in the challenging task of PET image denoising, MedGAN produced sharp denoised images in comparison to the highly blurred results of the other methods. Qualitative comparisons are highly subjective and can not be relied solely upon. Nevertheless, quantitative assessments, given in Table II, also reflect the above conclusions with MedGAN outperforming the current state-of-the-art methods on the different medical translation tasks. In PET-CT translation, MedGAN surpassed the other methods in all metrics by a significant margin, with the MSE reaching 264.6 in comparison to 288.6 achieved by the ID-CGAN, the second best performing method on this task. Similarly, MedGAN surpassed the scores achieved on the remaining two tasks with the exception of minor differences in the PSNR on the MR motion correction task and the VIF and UQI scores on the PET denoising task. Again, these minor differences are due to the lack of existing reliable metrics that asses translated or generated images according to the basis of humans perceptual judgement. However, the recently introduced LPIPS metric is one of the current state-of-the-art metrics which attempts to achieve this by utilizing deep pre-trained neural networks. Examination of the LPIPS scores across the different medical translation tasks emphasizes how MedGAN outperforms its competitors in terms of perceptual quality. Additional results are presented in Appendix B.

To judge the subjective perceptual performance of

MedGAN, we conducted a perceptual study in which 5 experienced radiologists rated the fidelity of the translated images in the three carried out medical translation tasks against the original ground truth images as well as the pix2pix outputs. MedGAN achieved a significantly higher performance compared to the current pix2pix model. This emphasizes the significant leap in performance achieved by MedGAN in comparison to prior general purpose translation frameworks. Additionally, no pix2pix translated images were classified by radiologists as real images in comparison with the ground truth, whereas 25.3 % of MedGAN outputs were classified as real. This score is quite remarkable since it reflects the level of realism achievable through the MedGAN framework.

## 6 CONCLUSION

MedGAN is an end-to-end general purpose solution for medical image translation tasks. The MedGAN framework was compared against its individual loss components showing that it is more than the sum of its parts. Moreover, to showcase the applicability of MedGAN as a general purpose solution for medical translation, MedGAN was applied on three novel and challenging applications: PET-CT translation, MR motion correction and PET denoising. Qualitative and quantitative comparisons using multiple scoring metrics with current state-of-the-art translation techniques such as pix2pix, ID-CGAN, PAN and Fila-sGAN emphasized MedGAN's superior performance. Finally, the subjective perceptual performance and fidelity of the translated results via MedGAN was attested and compared to the pix2pix framework by 5 experienced radiologists.

As a future work, we plan to investigate the performance of MedGAN for each specific application more thoroughly. For example, we plan to train MedGAN on uncorrected PET-CT data and investigate the usability of the synthetic CTs for PET independent attenuation correction. Moreover, we plan to explore the applicability of utilizing retrospectively corrected MR images in a large cohort for segmentation and organ volume calculation. Moreover, we plan to utilize an independent dataset of whole-body MR images for pre-training the required feature extractor.

## REFERENCES

- [1] J. G. Colsher, J. Hsieh, J. B. Thibault, A. Lonn, T. Pan, S. J. Lokitz, and T. G. Turkington, "Ultra low dose ct for attenuation correction in pet/ct," in *2008 IEEE Nuclear Science Symposium Conference Record*, Oct 2008, pp. 5506–5511.
- [2] O. Mark, S. J. H., S. Anil, and J. D. A., "High resolution gelāšdosimetry by opticalāšct and mr scanning," *Medical Physics*, vol. 28, no. 7, pp. 1436–1445. [Online]. Available: [aapm.onlinelibrary.wiley.com/doi/abs/10.1111/1.1380430](http://aapm.onlinelibrary.wiley.com/doi/abs/10.1111/1.1380430)
- [3] T. Huynh, Y. Gao, J. Kang, L. Wang, P. Zhang, J. Lian, and D. Shen, "Estimating CT image from MRI data using structured random forest and auto-context model," *IEEE Transactions on Medical Imaging*, vol. 35, pp. 174–183, 2016.
- [4] L. Zhong, L. Lin, Z. Lu, Y. Wu, Z. Lu, M. Huang, W. Yang, and Q. Feng, "Predict CT image from MRI data using KNN-regression with learned local descriptors," in *2016 IEEE 13th International Symposium on Biomedical Imaging (ISBI)*, April 2016, pp. 743–746.

- [5] W. Yang, L. Zhong, Y. Chen, L. Lin, Z. Lu, S. Liu, Y. Wu, Q. Feng, and W. Chen, "Predicting CT image from MRI data through feature matching with learned nonlinear local descriptors," *IEEE Transactions on Medical Imaging*, vol. 37, no. 4, pp. 977–987, April 2018.
- [6] T. Kustner, M. Schwartz, P. Martirosian, S. Gatidis, F. Seith, C. Gilliam, T. Blu, H. Fayad, D. Visvikis, F. Schick, B. Yang, H. Schmidt, and N. Schwenzer, "MR-based respiratory and cardiac motion correction for PET imaging," *Medical image analysis*, vol. 42, pp. 129–144, 2017.
- [7] A. Rueda, N. Malpica, and E. Romero, "Single-image super-resolution of brain MR images using overcomplete dictionaries," vol. 17, p. 113A–S132, 10 2012.
- [8] G. J. S. Litjens, T. Kooi, B. E. Bejnordi, A. A. A. Setio, F. Ciompi, M. Ghafoorian, J. van der Laak, B. van Ginneken, and C. I. Sánchez, "A survey on deep learning in medical image analysis," *Medical image analysis*, vol. 42, pp. 60–88, 2017.
- [9] H. C. Shin, H. R. Roth, M. Gao, L. Lu, Z. Xu, I. Nogues, J. Yao, D. Mollura, and R. M. Summers, "Deep convolutional neural networks for computer-aided detection: CNN architectures, dataset characteristics and transfer learning," *IEEE Transactions on Medical Imaging*, vol. 35, no. 5, pp. 1285–1298, May 2016.
- [10] Q. Dou, H. Chen, L. Yu, J. Qin, and P. A. Heng, "Multi-level contextual 3-D CNNs for false positive reduction in pulmonary nodule detection," *IEEE Transactions on Biomedical Engineering*, vol. 64, no. 7, pp. 1558–1567, July 2017.
- [11] M. Havaei, A. Davy, D. Warde-Farley, A. Biard, A. Courville, Y. Bengio, C. Pal, P.-M. Jodoin, and H. Larochelle, "Brain tumor segmentation with deep neural networks," vol. 35, 05 2015.
- [12] K. Kamnitsas, C. Ledig, V. Newcombe, J. P. Simpson, A. Kane, D. Menon, D. Rueckert, and B. Glocker, "Efficient multi-scale 3D CNN with fully connected CRF for accurate brain lesion segmentation," vol. 36, 03 2016.
- [13] S. Miao, Z. J. Wang, and R. Liao, "A CNN regression approach for real-time 2D/3D registration," *IEEE Transactions on Medical Imaging*, vol. 35, no. 5, pp. 1352–1363, May 2016.
- [14] H. Chen, Y. Zhang, M. K. Kalra, F. Lin, Y. Chen, P. Liao, J. Zhou, and G. Wang, "Low-Dose CT with a residual encoder-decoder convolutional neural network," vol. 36, pp. 2524–2535, 06 2017.
- [15] K. Bahrami, F. Shi, I. Rekik, and D. Shen, "Convolutional neural network for reconstruction of 7T-like images from 3T MRI using appearance and anatomical features," in *LABELS/DLMIA@MICCAI*, 2016.
- [16] O. Oktay, W. Bai, M. C. H. Lee, R. Guerrero, K. Kamnitsas, J. Caballero, A. de Marvao, S. A. Cook, D. P. O'Regan, and D. Rueckert, "Multi-input cardiac image super-resolution using convolutional neural networks," in *MICCAI*, 2016.
- [17] Y. LeCun, Y. Bengio, and G. Hinton, "Deep learning," vol. 521, pp. 436–44, 05 2015.
- [18] I. J. Goodfellow, J. Pouget-Abadie, M. Mirza, B. Xu, D. Warde-Farley, S. Ozair, A. C. Courville, and Y. Bengio, "Generative adversarial nets," in *NIPS*, 2014.
- [19] D. P Kingma and M. Welling, "Auto-Encoding variational bayes," 12 2014.
- [20] D. J. Rezende, S. Mohamed, and D. Wierstra, "Stochastic backpropagation and approximate inference in deep generative models," in *Proceedings of the 31st International Conference on Machine Learning*, ser. Proceedings of Machine Learning Research, E. P. Xing and T. Jebara, Eds., vol. 32, no. 2. Beijing, China: PMLR, 22–24 Jun 2014, pp. 1278–1286. [Online]. Available: <http://proceedings.mlr.press/v32/rezende14.html>
- [21] J. Bao, D. Chen, F. Wen, H. Li, and G. Hua, "CVAE-GAN: Fine-Grained image generation through asymmetric training," pp. 2764–2773, 10 2017.
- [22] J. J. Zhao, M. Mathieu, and Y. LeCun, "Energy-based generative adversarial network," *ICLR*, 2016.
- [23] A. Creswell, T. White, V. Dumoulin, K. Arulkumaran, B. Sen-gupta, and A. A. Bharath, "Generative adversarial networks: An overview," *IEEE Signal Processing Magazine*, vol. 35, no. 1, pp. 53–65, Jan 2018.
- [24] Y. Hong, U. Hwang, J. Yoo, and S. Yoon, "How generative adversarial nets and its variants work: An overview of GAN," *CoRR*, vol. abs/1711.05914, 2017. [Online]. Available: <http://arxiv.org/abs/1711.05914>
- [25] A. Radford, L. Metz, and S. Chintala, "Unsupervised representation learning with deep convolutional generative adversarial networks," *ICLR*, 11 2016.
- [26] M. Arjovsky and L. Bottou, "Towards principled methods for training generative adversarial networks," *ICLR*, vol. abs/1701.04862, 2017.
- [27] M. Arjovsky, S. Chintala, and L. Bottou, "Wasserstein generative adversarial networks," in *Proceedings of the 34th International Conference on Machine Learning*, ser. Proceedings of Machine Learning Research, D. Precup and Y. W. Teh, Eds., vol. 70. International Convention Centre, Sydney, Australia: PMLR, 06–11 Aug 2017, pp. 214–223. [Online]. Available: <http://proceedings.mlr.press/v70/arjovsky17a.html>
- [28] I. Gulrajani, F. Ahmed, M. Arjovsky, V. Dumoulin, and A. C. Courville, "Improved training of wasserstein GANs," *NIPS*, vol. abs/1704.00028, 2017. [Online]. Available: <http://arxiv.org/abs/1704.00028>
- [29] X. Wei, B. Gong, Z. Liu, W. Lu, and W. Chen, "Improving the improved training of wasserstein GANs: A consistency term and its dual effect," *ICLR*, vol. abs/1803.01541, 2018.
- [30] C. Li, W. Chang, Y. Cheng, Y. Yang, and B. Póczos, "MMD GAN: towards deeper understanding of moment matching network," *NIPS*, vol. abs/1705.08584, 2017. [Online]. Available: <http://arxiv.org/abs/1705.08584>
- [31] M. BiÅdkowski, D. J. Sutherland, M. Arbel, and A. Gretton, "Demystifying MMD GANs," *ICLR*, 01 2018.
- [32] N. Kodali, J. D. Abernethy, J. Hays, and Z. Kira, "How to train your DRAGAN," *CoRR*, vol. abs/1705.07215, 2017. [Online]. Available: <http://arxiv.org/abs/1705.07215>
- [33] T. Miyato, T. Kataoka, M. Koyama, and Y. Yoshida, "Spectral normalization for generative adversarial networks," *ICLR*, vol. abs/1802.05957, 2018. [Online]. Available: <http://arxiv.org/abs/1802.05957>
- [34] D. Berthelot, T. Schumm, and L. Metz, "BEGAN: boundary equilibrium generative adversarial networks," *ICLR*, vol. abs/1703.10717, 2017. [Online]. Available: <http://arxiv.org/abs/1703.10717>
- [35] T. Karras, T. Aila, S. Laine, and J. Lehtinen, "Progressive growing of GANs for improved quality, stability, and variation," *ICLR*, vol. abs/1710.10196, 2017. [Online]. Available: <http://arxiv.org/abs/1710.10196>
- [36] C. Ledig, L. Theis, F. Huszar, J. Caballero, A. P. Aitken, A. Tejani, J. Totz, Z. Wang, and W. Shi, "Photo-realistic single image super-resolution using a generative adversarial network," *CVPR*, vol. abs/1609.04802, 2016. [Online]. Available: <http://arxiv.org/abs/1609.04802>
- [37] T. Salimans, I. J. Goodfellow, W. Zaremba, V. Cheung, A. Radford, and X. Chen, "Improved techniques for training GANs," in *NIPS*, 2016.
- [38] H. Zhang, V. Sindagi, and V. M. Patel, "Image de-raining using a conditional generative adversarial network," *CoRR*, vol. abs/1701.05957, 2017. [Online]. Available: <http://arxiv.org/abs/1701.05957>
- [39] H. Zhang, T. Xu, H. Li, S. Zhang, X. Huang, X. Wang, and D. N. Metaxas, "StackGAN: Text to photo-realistic image synthesis with stacked generative adversarial networks," *ICCV*, vol. abs/1612.03242, 2016. [Online]. Available: <http://arxiv.org/abs/1612.03242>
- [40] P. Isola, J. Zhu, T. Zhou, and A. A. Efros, "Image-to-image translation with conditional adversarial networks," *CVPR*, vol. abs/1611.07004, 2016. [Online]. Available: <http://arxiv.org/abs/1611.07004>
- [41] C. Wang, C. Xu, C. Wang, and D. Tao, "Perceptual adversarial networks for image-to-image transformation," *IEEE Transactions on Image Processing*, vol. 27, no. 8, pp. 4066–4079, Aug 2018.
- [42] H. Zhao, H. Li, and L. Cheng, "Synthesizing filamentary structured images with gans," *CoRR*, vol. abs/1706.02185, 2017.
- [43] J. Johnson, A. Alahi, and F. Li, "Perceptual losses for real-time style transfer and super-resolution," *CoRR*, vol. abs/1603.08155, 2016. [Online]. Available: <http://arxiv.org/abs/1603.08155>
- [44] J. Zhu, T. Park, P. Isola, and A. A. Efros, "Unpaired image-to-image translation using cycle-consistent adversarial networks," *ICCV*, vol. abs/1703.10593, 2017. [Online]. Available: <http://arxiv.org/abs/1703.10593>

- [45] T. Kim, M. Cha, H. Kim, J. K. Lee, and J. Kim, “Learning to discover cross-domain relations with generative adversarial networks,” *ICML*, vol. abs/1703.05192, 2017. [Online]. Available: <http://arxiv.org/abs/1703.05192>
- [46] D. Nie, R. Trullo, J. Lian, L. Wang, C. Petitjean, S. Ruan, Q. Wang, and D. Shen, “Medical image synthesis with deep convolutional adversarial networks,” *IEEE Transactions on Biomedical Engineering*, pp. 1–1, 2018.
- [47] J. M. Wolterink, A. M. Dinkla, M. H. F. Savenije, P. R. Seevinck, C. A. T. van den Berg, and I. Isgrum, “Deep MR to CT synthesis using unpaired data,” *MICCAI*, vol. abs/1708.01155, 2017. [Online]. Available: <http://arxiv.org/abs/1708.01155>
- [48] J. Wolterink, T. Leiner, M. A. Viergever, and I. Isgrum, “Generative adversarial networks for noise reduction in low-dose CT,” vol. PP, pp. 1–1, 05 2017.
- [49] Q. Yang, P. Yan, Y. Zhang, H. Yu, Y. Shi, X. Mou, M. K. Kalra, Y. Zhang, L. Sun, and G. Wang, “Low-dose CT image denoising using a generative adversarial network with wasserstein distance and perceptual loss,” *IEEE Transactions on Medical Imaging*, vol. 37, no. 6, pp. 1348–1357, June 2018.
- [50] G. Yang, S. Yu, H. Dong, G. Slabaugh, P. L. Dragotti, X. Ye, F. Liu, S. Arridge, J. Keegan, Y. Guo, and D. Firmin, “DA-GAN: deep de-aliasing generative adversarial networks for fast compressed sensing MRI reconstruction,” *IEEE Transactions on Medical Imaging*, vol. 37, no. 6, pp. 1310–1321, June 2018.
- [51] T. M. Quan, T. Nguyen-Duc, and W. K. Jeong, “Compressed sensing MRI reconstruction using a generative adversarial network with a cyclic loss,” *IEEE Transactions on Medical Imaging*, vol. 37, no. 6, pp. 1488–1497, June 2018.
- [52] A. Ben-Cohen, E. Klang, S. P. Raskin, S. Soffer, S. Ben-Haim, E. Konen, M. M. Amitai, and H. Greenspan, “Cross-modality synthesis from CT to PET using FCN and GAN networks for improved automated lesion detection,” *CoRR*, vol. abs/1802.07846, 2018. [Online]. Available: <http://arxiv.org/abs/1802.07846>
- [53] D. Nie, R. Trullo, J. Lian, L. Wang, C. Petitjean, S. Ruan, Q. Wang, and D. Shen, “Medical image synthesis with deep convolutional adversarial networks,” *IEEE Transactions on Biomedical Engineering*, pp. 1–1, 2018.
- [54] Q. Yang, N. Li, Z. Zhao, X. Fan, E. I.-C. Chang, and Y. Xu, “MRI image-to-image translation for cross-modality image registration and segmentation,” *CoRR*, vol. abs/1801.06940, 2018.
- [55] S. U. H. Dar, M. Yurt, L. Karacan, A. Erdem, E. Erdem, and T. Çukur, “Image synthesis in multi-contrast MRI with conditional generative adversarial networks,” *CoRR*, vol. abs/1802.01221, 2018. [Online]. Available: <http://arxiv.org/abs/1802.01221>
- [56] K. He, X. Zhang, S. Ren, and J. Sun, “Deep residual learning for image recognition,” in *2016 IEEE Conference on Computer Vision and Pattern Recognition (CVPR)*, June 2016, pp. 770–778.
- [57] D. Pathak, P. Krähenbühl, J. Donahue, T. Darrell, and A. A. Efros, “Context encoders: Feature learning by inpainting,” *CVPR*, vol. abs/1604.07379, 2016. [Online]. Available: <http://arxiv.org/abs/1604.07379>
- [58] R. Zhang, P. Isola, and A. Efros, “Colorful image colorization,” *ECCV*, vol. 9907, pp. 649–666, 10 2016.
- [59] J. Johnson, A. Alahi, and F. Li, “Perceptual losses for real-time style transfer and super-resolution,” *CoRR*, vol. abs/1603.08155, 2016. [Online]. Available: <http://arxiv.org/abs/1603.08155>
- [60] L. A. Gatys, A. S. Ecker, and M. Bethge, “Image style transfer using convolutional neural networks,” in *2016 IEEE Conference on Computer Vision and Pattern Recognition (CVPR)*, June 2016, pp. 2414–2423.
- [61] O. Ronneberger, P. Fischer, and T. Brox, “U-net: Convolutional networks for biomedical image segmentation,” in *Medical Image Computing and Computer-Assisted Intervention – MICCAI 2015*, N. Navab, J. Hornegger, W. M. Wells, and A. F. Frangi, Eds. Cham: Springer International Publishing, 2015, pp. 234–241.
- [62] K. Simonyan and A. Zisserman, “Very deep convolutional networks for large-scale image recognition,” *ICLR*, vol. abs/1409.1556, 2014. [Online]. Available: <http://arxiv.org/abs/1409.1556>
- [63] D. P. Kingma and J. Ba, “Adam: A method for stochastic optimization,” *ICLR*, vol. abs/1412.6980, 2014. [Online]. Available: <http://arxiv.org/abs/1412.6980>
- [64] D. Ulyanov, A. Vedaldi, and V. S. Lempitsky, “Instance normalization: The missing ingredient for fast stylization,” *CoRR*, vol. abs/1607.08022, 2016. [Online]. Available: <http://arxiv.org/abs/1607.08022>
- [65] T. Küstner, M. Jandt, A. Liebgott, L. Mauch, P. Martirosian, F. Bamberg, K. Nikolaou, S. Gatidis, B. Yang, and F. Schick, “Motion artifact quantification and localization for whole-body MRI,” in *Proceedings of the International Society for Magnetic Resonance in Medicine (ISMRM)*, Paris, France, Jun. 2018.
- [66] T. Küstner, A. Liebgott, L. Mauch, P. Martirosian, F. Bamberg, K. Nikolaou, B. Yang, F. Schick, and S. Gatidis, “Automated reference-free detection of motion artifacts in magnetic resonance images,” *Magnetic Resonance Materials in Physics, Biology and Medicine*, vol. 31, no. 2, pp. 243–256, Apr 2018. [Online]. Available: <https://doi.org/10.1007/s10334-017-0650-z>
- [67] A. Borji, “Pros and cons of GAN evaluation measures,” *CoRR*, vol. abs/1802.03446, 2018. [Online]. Available: <http://arxiv.org/abs/1802.03446>
- [68] Z. Wang, A. C. Bovik, H. R. Sheikh, and E. P. Simoncelli, “Image quality assessment: from error visibility to structural similarity,” *IEEE Transactions on Image Processing*, vol. 13, no. 4, pp. 600–612, April 2004.
- [69] H. R. Sheikh and A. C. Bovik, “Image information and visual quality,” *IEEE Transactions on Image Processing*, vol. 15, no. 2, pp. 430–444, Feb 2006.
- [70] Z. Wang and A. C. Bovik, “A universal image quality index,” *IEEE Signal Processing Letters*, vol. 9, no. 3, pp. 81–84, March 2002.
- [71] R. Zhang, P. Isola, A. A. Efros, E. Shechtman, and O. Wang, “The unreasonable effectiveness of deep features as a perceptual metric,” *CVPR*, vol. abs/1801.03924, 2018. [Online]. Available: <http://arxiv.org/abs/1801.03924>

**APPENDIX A**  
**Analysis of Generator Architecture**

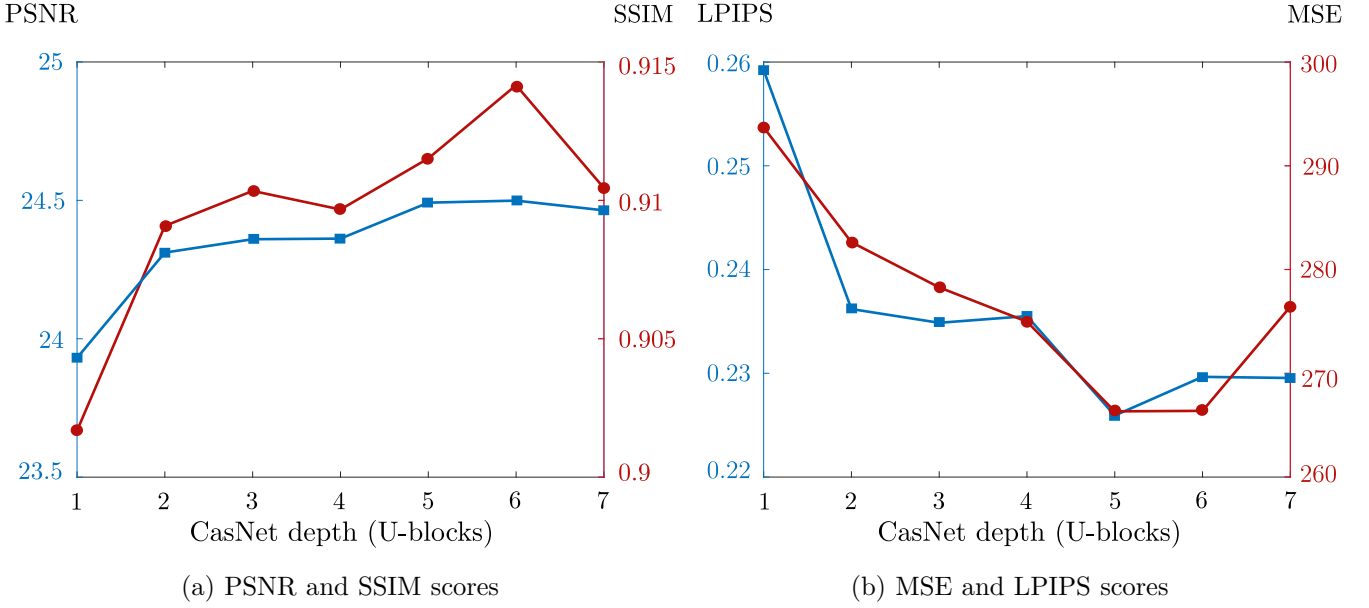


Fig. 6: Quantitative comparison of performance of a pix2pix network using CasNet versus the number of U-blocks.

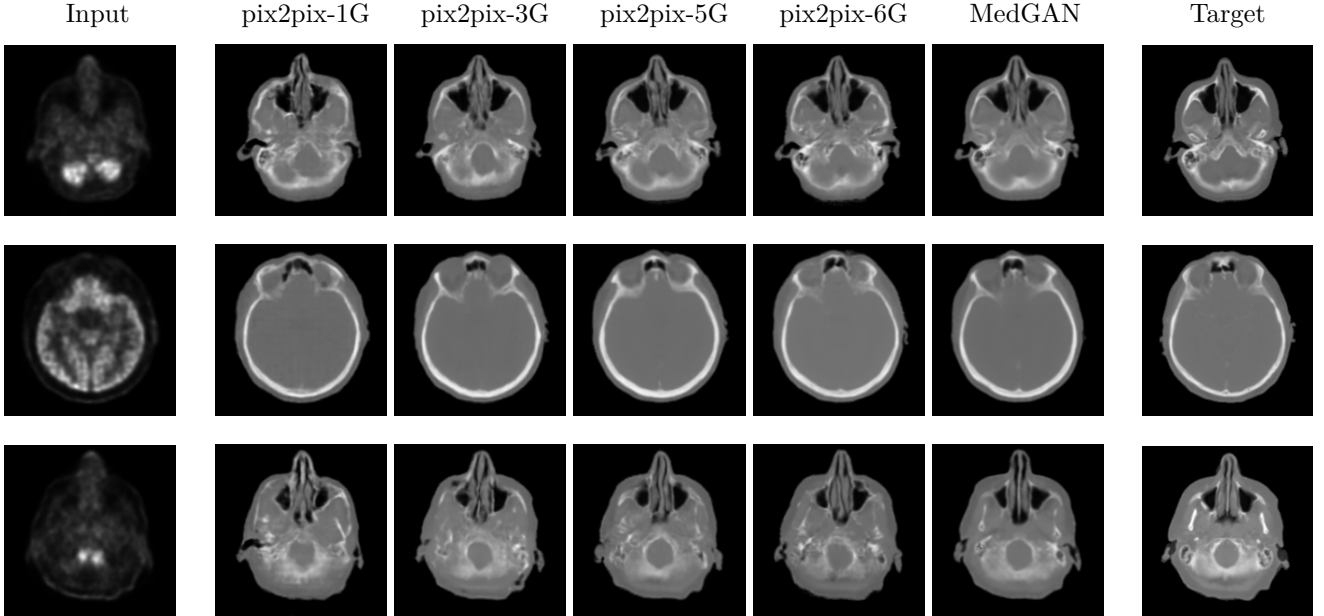


Fig. 7: Comparison of pix2pix with a CasNet of 1, 3, 5 and 6 U-blocks respectively versus the MedGAN framework.

To investigate the performance of the proposed CasNet architecture, we implemented pix2pix models utilizing CasNet with different block depth, from 1 to 7 U-blocks. Quantitative performance is presented in Fig. 6. It can be seen that as the CasNet utilizes greater capacity through a larger concatenation of U-blocks, quantitative performance increases significantly up until the 6th U-block. Beyond this point, performance either saturates,

e.g. PSNR and MSE, or starts to degrade, in the case of SSIM and LPIPS scores. Further investigations are required to determine the optimum depth of CasNet. Fig. 7 illustrates the effect of CasNet on the translated images by pix2pix of different CasNet depth in comparison to MedGAN (6 U-blocks). It can be seen that as the number of U-blocks increases visual quality of translated images is significantly improved.

**APPENDIX B**  
**Extra Results**

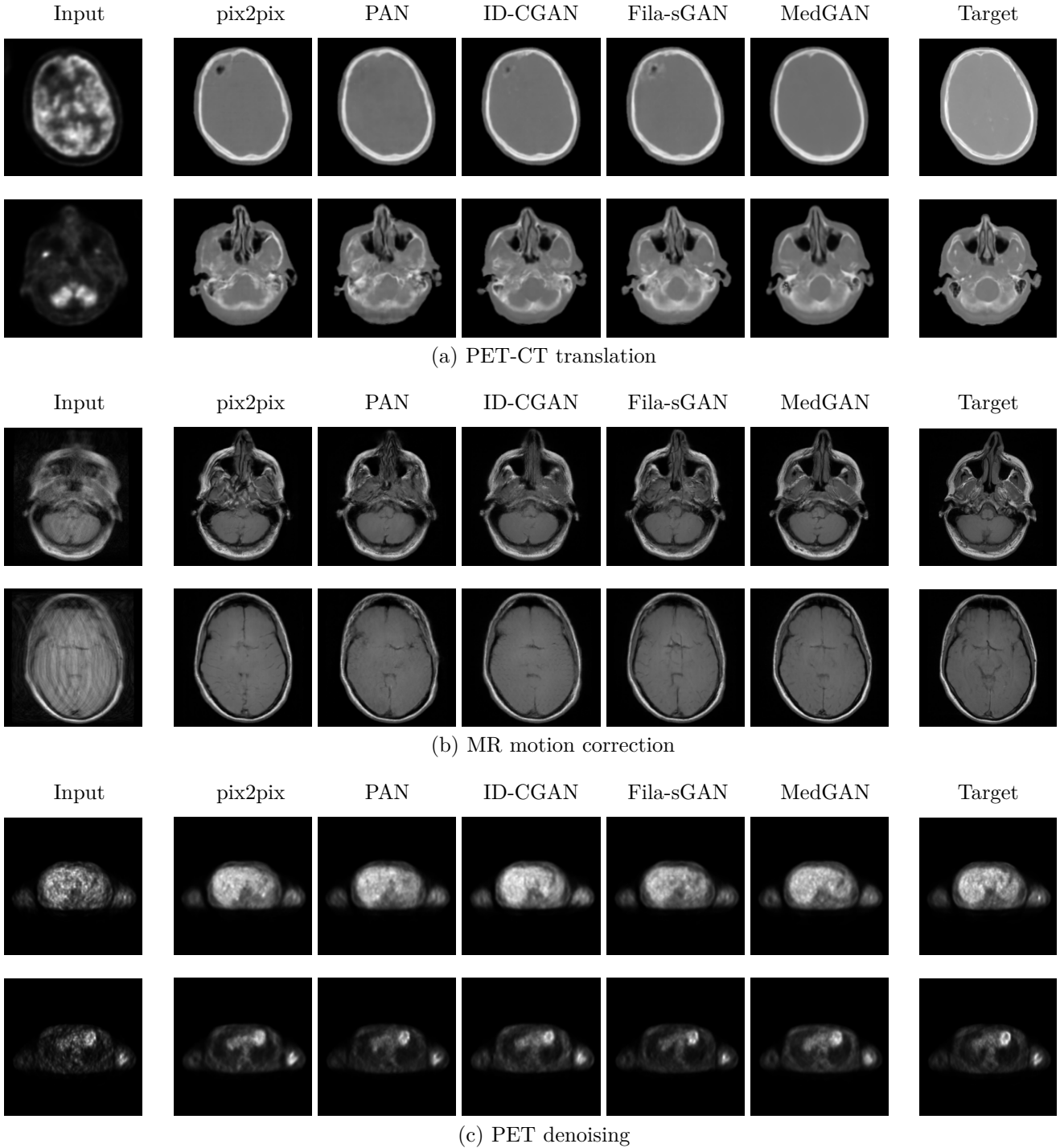


Fig. 8: Extra results comparing MedGAN and state-of-the-art techniques on various medical image translation tasks.